Pressure studies of subthreshold photoionization: CH_3I perturbed by CF_4 and *c*-C_4F_8

C. M. Evans [a,b] and G. L. Findley [b,*]

[a] *Center for Advanced Microstructures and Devices (CAMD) and Department of Chemistry, Louisiana State University, Baton Rouge, LA 70803, USA*

[b] *Department of Chemistry, University of Louisiana at Monroe, Monroe, LA 71209, USA*

Submitted 9 October 2000

Abstract

Subthreshold photoionization spectra of CH_3I perturbed by CF_4 and *c*-C_4F_8 for variable CH_3I number density ρ_{CH_3I} and perturber number density ρ_P are presented. The ρ_{CH_3I} and ρ_P dependence of the subthreshold structure is discussed in terms of the excited-state processes of electron attachment and associative ionization. The effective rate constants for these processes are determined from the variation in the subthreshold photocurrent as a function of ρ_{CH_3I} and ρ_P. These constants are then analyzed with respect to the properties of the excited CH_3I Rydberg state. The variation in the effective rate constants is discussed in terms of ground-state perturber properties.

1. Introduction

Methyl iodide (CH_3I) has served as a convenient probe in many photoionization studies of dopant (D)/perturber (P) interactions [1-14] because of the low first ionization threshold and sharp autoionization structure of this dopant. In many CH_3I/P systems [1-8,11,12,14], photoionization structure has been observed to occur at energies lower than the unperturbed CH_3I ionization threshold. This subthreshold photoionization structure has been interpreted as arising from the excited-state processes of electron attachment and associative ionization [11,12,14]. Moreover, since this structure tracks the photoabsorption of discrete CH_3I Rydberg states in the same energy region, the subthreshold structure has been used to evaluate the zero-kinetic-energy electron scattering lengths in highly absorbing perturber media [6-8,11].

In recent studies of the subthreshold photoionization of pure CH_3I [1-4,11,14], CH_3I/P (P = Ar [12,14], N_2 [12], CO_2 [12] and SF_6 [11,14]), C_2H_5I/SF_6 [14,15] and C_6H_6/SF_6 [14,15], two possible pathways leading to subthreshold photocurrent have been proposed. The first pathway, namely [11,14,15]

$$D^* + P \rightarrow D^+ + P^- \quad (1)$$

$$D^* + P \rightarrow DP^+ + e^- , \quad (2)$$

involves direct D/P interactions in the form of electron attachment to the perturber and heteromolecular D/P dimerization, respectively. (In Eqs. (1) and (2), D^* is a discrete Rydberg state of the dopant molecule.) In contrast, the second pathway, namely [11,12,14,15]

$$D^* + D \rightarrow D^+ + D^- \quad (3)$$

* Corresponding author. E-mail: chfindley@ulm.edu

$$D^* + D \rightarrow D_2^+ + e^- \quad (4)$$

$$D^* + D + P \rightarrow D_2^+ + P + e^- , \quad (5)$$

invokes only indirect D/P interactions in the form of perturber-stabilized homomolecular dopant dimerization (i.e., Eq. (5)) [16].

For either of the above pathways, the total subthreshold photocurrent is given by a sum of two contributions, namely the photocurrent resulting from electron attachment and that resulting from associative ionization. Under the assumptions that (i) electron attachment is *saturated* (i.e., dependent only on the excited-state dopant number density ρ_{D^*}), and (ii) $\rho_{D^*} \propto \rho_D$ in the linear absorption regime, the total subthreshold photocurrent is [11,14,15]

$$i = k_{ea}^{(1)} \rho_D + k_{ai}^{(1)} \rho_D \rho_P \quad (6)$$

for pathway 1, and [11,12,14,15]

$$i = k_{ea}^{(2)} \rho_D + k_{ai}^{(2)} \rho_D^2 + k_{ai}'^{(2)} \rho_D^2 \rho_P \quad (7)$$

for pathway 2. In Eqs. (6) and (7), $k_{ea}^{(1,2)}$ is the effective rate constant for (saturated) electron attachment (i.e., Eqs. (1) and (3)); $k_{ai}^{(1,2)}$ is the associative ionization effective rate constant (i.e., Eqs. (2) and (4)); and $k_{ai}'^{(2)}$ is the effective rate constant for perturber-stabilized associative ionization (i.e., Eq. (5)).

Subthreshold photoionization structure has been observed in CH_3I/P (P = Ar and SF_6 [14]), for variable ρ_{CH_3I} and ρ_P, which is quadratically dependent on ρ_{CH_3I} and linearly dependent on ρ_P. For the cases of pure CH_3I [11,14] and CH_3I/Ar [12,14], this subthreshold structure was modeled solely within the confines of pathway 2. The CH_3I/SF_6 subthreshold photocurrent, however, proceeded through both pathways 1 and 2 simultaneously and, therefore, was modeled by the sum of Eqs. (6) and (7), or [11,14]

$$i = \left(k_{ai}^{(2)} \rho_D^2 + (k_{ea}^{(1)} + k_{ea}^{(2)}) \rho_D\right) + \left(k_{ai}'^{(2)} \rho_D^2 + k_{ai}^{(1)} \rho_D\right) \rho_P . \quad (8)$$

Since both ρ_{CH_3I} and ρ_P were varied systematically, the effective rate constants for electron attachment and associative ionization could be determined. The variations in these rate constants were shown to scale in a simple fashion with the electron affinity of the perturber ($k_{ea}^{(1)}$), the electron affinity of the dopant ($k_{ea}^{(2)}$), the ground-state polarizability of the dopant ($k_{ai}^{(2)}$), and the ground-state polarizability of the perturber ($k_{ai}^{(1)}$ and $k_{ai}'^{(2)}$) [14]. However, additional measurements of subthreshold photoionization for variable ρ_{CH_3I} and ρ_P for different perturbers are needed to test the wider applicability of pathways 1 and 2, and to continue to probe the dependencies of the effective rate constants upon perturber properties.

In the present paper, we present a systematic number density study of the subthreshold photoionization structure of CH_3I perturbed by CF_4 and *c*-C_4F_8. The perturber CF_4, which is widely used in plasma etching processes [17,18], was chosen because it does not form a stable ground-state anion [19]; therefore, subthreshold photocurrent should proceed through pathway 2 with no contribution from pathway 1. The perturber *c*-C_4F_8, which is also important in plasma etching [17,18], was selected because it has a moderate electron affinity; therefore, subthreshold photocurrent should be able to access pathway 1. As will be reported below, the subthreshold photocurrent in CH_3I/CF_4 can indeed be modeled by pathway 2, while CH_3I/*c*-C_4F_8 requires both pathways 1 and 2 in order to explain the dopant and perturber density dependence. By varying ρ_{CH_3I} and ρ_P (P = CF_4, *c*-C_4F_8) separately, we were able to determine the effective rate constants for electron attachment and associative ionization. Therefore, the effects of electron affinity (of D or P) on $k_{ea}^{(1,2)}$ and of the ground-state polarizability (of D or P) on $k_{ai}^{(1,2)}$ and $k_{ai}'^{(2)}$ are presented.

2. Experiment

Photoionization spectra were measured with monochromatized synchrotron radiation [20] having a resolution of 0.09 nm, or ~ 8 meV, in the spectral region of interest. This radiation entered a copper experimental cell [10,21], equipped with entrance and exit MgF_2 windows, that is capable of withstanding pressures of up to 100 bar. This cell, which possesses two parallel plate electrodes (stainless steel, 3 mm spacing) aligned perpendicular to the windows, was connected to a cryostat and heater system allowing the temperature to be controlled to within ± 1 K. The light path within the cell is 1.0 cm. The applied voltage was 100 V, and all photoionization spectra were current saturated (which was verified by measuring selected spectra at different applied voltages). Photocurrents within the cell were of the order of 10^{-10} A.

All photoionization spectra were measured at room temperature, excepted as noted below. The intensity of the synchrotron radiation exiting the monochromator was monitored by measuring the current across a Ni mesh intercepting the beam prior to the experimental cell. All photoionization spectra are normalized to this current. Furthermore, all spectra are intensity normalized to unity at the same CH_3I spectral feature above the $^2E_{3/2}$ [22] ionization threshold. (The spectral feature chosen for this normalization procedure was the same spectral feature used in a previous paper on CH_3I perturbed by Ar and SF_6 [14], to allow for comparisons with these earlier results.) Spectral peak areas were obtained by integrating a gaussian deconvolution of the subthreshold peaks [11,12,14,15].

CH_3I (Aldrich, 99.5%), CF_4 (Matheson Gas Products, 99.999%) and *c*-C_4F_8 (Matheson Gas Products, 99.98%) were used without further purification. Both the gas handling system and the procedures employed to ensure homogeneous mixing of the dopant and perturber have been described previously [10,23].

3. Results and discussion

We report subthreshold photoionization results for CH_3I perturbed by CF_4 and *c*-C_4F_8 for variations in both ρ_{CH_3I} and ρ_P. For the sake of brevity, however, we present only representative subthreshold photoionization spectra for each CH_3I/P system for a chosen ρ_P (varying ρ_{CH_3I}) and a chosen ρ_{CH_3I} (varying ρ_P). As was the case for CH_3I/P (P = Ar [12], N_2 [12], CO_2 [12], SF_6 [11]), we observed no temperature effect on the relative intensities of the subthreshold photoionization structure, thereby ruling out vibrational autoionization as a possible subthreshold photoionization mechanism [9]. The absence of any temperature dependence in the present case was verified by measuring subthreshold photoionization spectra for various CH_3I/P (P = CF_4, *c*-C_4F_8) sample pressures for at least three temperatures in the range of 0°C to 80°C.

In Figs. 1a and 1a′, subthreshold photoionization spectra of CH_3I/CF_4 are presented at constant ρ_{CF_4} and at constant ρ_{CH_3I}, respectively, and the peak areas obtained from these spectra are plotted versus ρ_{CH_3I} and ρ_{CF_4} in Figs. 1b and 1b′, respectively. The quadratic dependence of the subthreshold photocurrent on ρ_{CH_3I} (cf. Fig. 1b), coupled with the linear dependence of this structure on ρ_{CF_4} (cf. Fig. 1b′), leads us to conclude that the subthreshold photocurrent arises via pathway 2.

In Figs 2a and 2a′, subthreshold photoionization spectra of CH_3I/*c*-C_4F_8 are presented at constant $\rho_{c\text{-}C4F8}$ and ρ_{CH_3I}, respectively, and the peak areas obtained from these spectra are plotted versus ρ_{CH_3I} and $\rho_{c\text{-}C_4F_8}$ in Fig. 2b and 2b′, respectively. As in the case of CH_3I/CF_4, the quadratic dependence of this subthreshold structure on ρ_{CH_3I} (cf. Fig. 2b), and the linear dependence on $\rho_{c\text{-}C_4F_8}$ (cf. Fig. 2b′), indicates that pathway 2 is accessible. However, the lower onset energy observed for CH_3I/*c*-C_4F_8 in

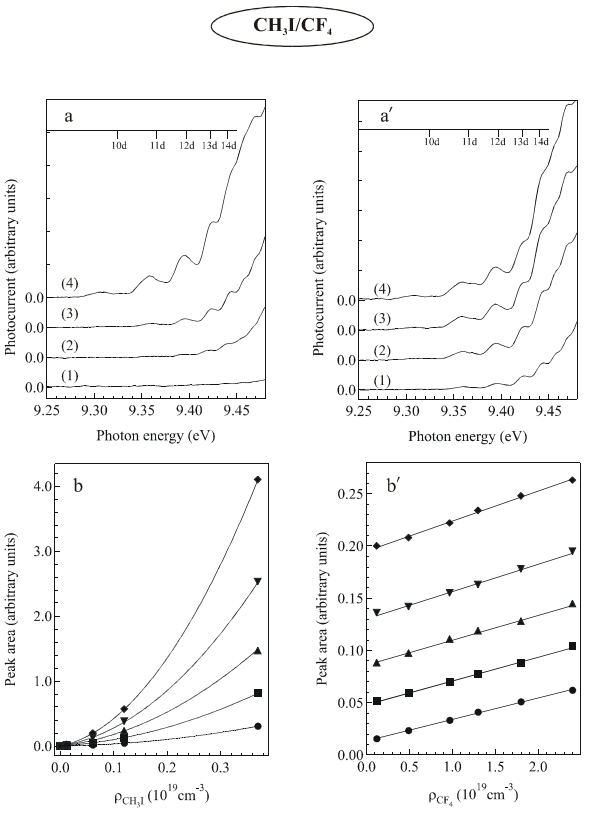

Fig. 1. Subthreshold photoionization of CH_3I/CF_4: **(a)** subthreshold photoionization spectra of varying ρ_{CH_3I} (10^{19}cm^{-3}) perturbed by 0.12 × 10^{19} cm^{-3} CF_4: (1) 0.00024, (2) 0.012, (3) 0.061, and (4) 0.37. **(a′)** Subthreshold photoionization spectra of 0.061 × 10^{19} cm^{-3} CH_3I perturbed by varying ρ_{CF_4} (10^{19}cm^{-3}): (1) 0.12, (2) 0.97, (3) 1.8, and (4) 2.4. (b) Peak areas (by gaussian fits to the photoionization spectra) for the subthreshold photoionization structure in **(a)** plotted vs. ρ_{CH_3I}. **(b′)** Peak areas (by gaussian fits to the photoionization spectra) for the subthreshold photoionization structure in **(a′)** plotted vs. ρ_{CF_4}. In **(a)** and **(a′)**: each spectrum is intensity normalized to unity at the same spectral feature above $^2E_{3/2}$ ionization threshold. In **(b)** and **(b′)**: (●) 10d, (■) 11d, (▲) 12d, (▼) 13d, and (◆) 14d. The solid lines represent least-square second-order polynomial fits to Eq. (7).

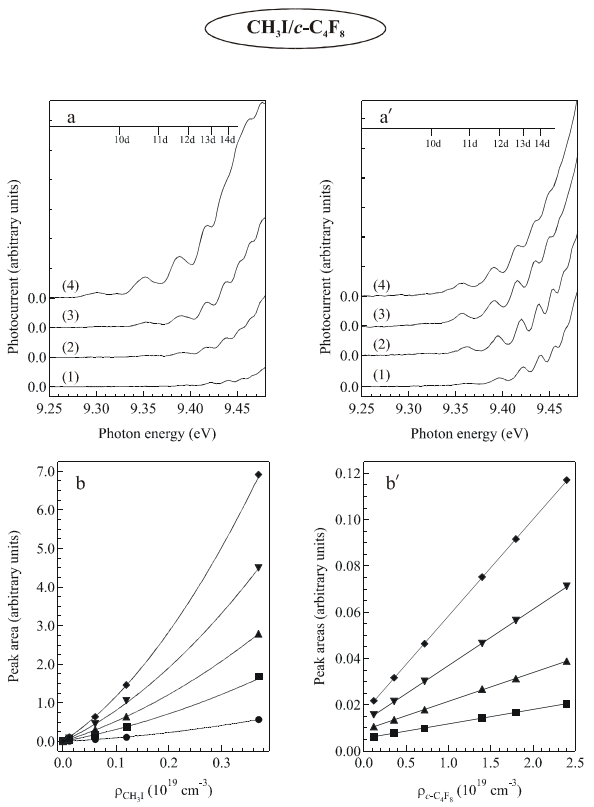

Fig. 2. Subthreshold photoionization of $CH_3I/c\text{-}C_4F_8$: **(a)** Subthreshold photoionization spectra of varying ρ_{CH_3I} (10^{19}cm^{-3}) perturbed by 0.12 × 10^{19} cm^{-3} c-C_4F_8: (1) 0.00024, (2) 0.012, (3) 0.061, and (4) 0.37. **(a′)** Subthreshold photoionization spectra of 0.00024 × 10^{19} cm^{-3} CH_3I perturbed by varying $\rho_{c\text{-}C_4F_8}$ (10^{19}cm^{-3}): (1) 0.12, (2) 0.72, (3) 1.8, and (4) 2.4. **(b)** Peak areas (obtained from gaussian fits to the photoionization spectra) for the subthreshold photoionization structure in **(a)** plotted vs. ρ_{CH_3I}. **(b′)** Peak areas (obtained from gaussian fits to the photoionization spectra) for the subthreshold photoionization structure in **(a′)** plotted vs. $\rho_{c\text{-}C_4F_8}$. In **(a)** and **(a′)**: each spectrum is intensity normalized to unity at the same spectral feature above $^2E_{3/2}$ ionization threshold. In **(b)** and **(b′)**: (●) 10d, (■) 11d, (▲) 12d, (▼) 13d, and (◆) 14d. The solid lines represent least-square second-order polynomial fits to Eq. (8).

comparison to CH_3I/CF_4 when ρ_{CH_3I} is small suggests that pathway 1 is also available. Therefore, accurate modeling of the $CH_3I/c\text{-}C_4F_8$ subthreshold photocurrent over the entire density range should require the use of Eq. (8),

$$i = b_0 + b_1 \rho_P^2 , \qquad (11)$$

The effective rate constants can be determined by examining the density dependence of the subthreshold photocurrent when ρ_P is varied at different constant values of ρ_{CH_3I}. In this case, the total subthreshold photocurrent for pathway 2 (i.e., Eq. (7)) and for the sum of the two pathways (i.e., Eq. (8)) reduces to the same form, namely

$$i = b_0 + b_1 \rho_P . \qquad (9)$$

The ρ_{CH_3I} dependence of the regression coefficients b_0 and b_1 differs significantly for each pathway, however. For pathway 2, the coefficients are

$$b_0 = k_{ea}^{(2)} \rho_{CH_3I} + k_{ai}^{(2)} \rho_{CH_3I}^2 , \; b_1 = k_{ai}^{\prime(2)} \rho_{CH_3I}^2 , \qquad (10)$$

whereas for the sum of the two pathways, these coefficients are

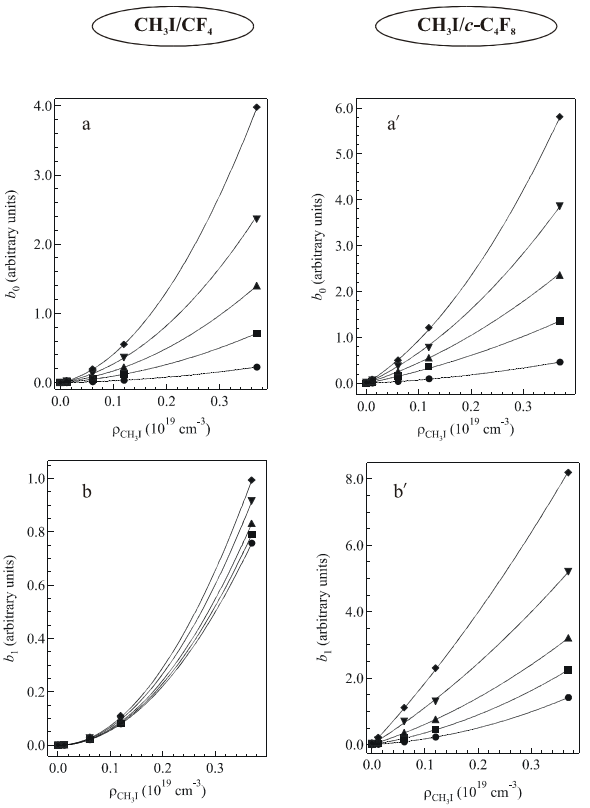

Fig. 3. **(a)** Constant and **(b)** linear regression coefficients for the subthreshold density dependence of CH_3I/CF_4 plotted vs. ρ_{CH_3I}. **(a′)** Constant and **(b′)** linear regression coefficients for the subthreshold density dependence of $CH_3I/c\text{-}C_4F_8$ plotted vs. ρ_{CH_3I}. (●) 10d, (■) 11d, (▲) 12d, (▼) 13d, and (◆) 14d. The solid lines represent least-square second-order polynomial fits to Eq. (10) (cf. Table 1) for CH_3I/CF_4 and to Eq. (11) (cf. Table 2) for $CH_3I/c\text{-}C_4F_8$. See text for discussion.

Table 1
(a) The constant regression coefficients b_0 and (b) the linear regression coefficients b_1 determined from a pressure study of the subthreshold photoionization structure of CH_3I/CF_4 as a function of ρ_{CH_3I} (10^{19} cm^{-3}).

a. b_0

ρ_{CH_3I}	10d	11d	12d	13d	14d
0.00024	0.00	0.00	0.00	0.00	0.00
0.012	0.00	0.0075	0.012	0.018	0.024
0.061	0.014	0.048	0.086	0.13	0.20
0.12	0.035	0.12	0.22	0.36	0.55
0.37	0.22	0.71	1.4	2.4	4.0
Effective rate constants (arbitrary units) [a]					
$k_{ea}^{(2)}$	0.15	0.58	0.92	1.3	1.7
$k_{ai}^{(2)}$	1.3	3.6	7.7	14	25

b. b_1

ρ_{CH_3I}	10d	11d	12d	13d	14d
0.00024	0.00	0.00	0.00	0.00	0.00
0.012	0.00	0.0082	0.0087	0.0094	0.010
0.061	0.021	0.023	0.024	0.026	0.029
0.12	0.080	0.083	0.089	0.095	0.11
0.37	0.76	0.79	0.83	0.92	0.99
Effective rate constant (arbitrary units) [a]					
$k_{ai}'^{(2)}$	5.5	5.8	6.1	6.7	7.3

[a]The effective rate constants $k_{ea}^{(2)}$, $k_{ai}^{(2)}$ and $k_{ai}'^{(2)}$ are for least-square second-order polynomial fits to Eq. (10), as shown in Figs. 3a and 3b.

Since pathway 2 was invoked to explain the subthreshold photoionization structure observed in CH_3I/CF_4 (cf. Fig. 1), the ρ_{CH_3I} dependence of the coefficients b_0 and b_1 should be given by Eq. (10). Therefore, if b_0 and b_1 are obtained for various values of ρ_{CH_3I}, and if b_0 and b_1 show the correct quadratic dependence upon ρ_{CH_3I}, then pathway 2 has been substantiated, and the effective rate constants $k_{ea}^{(2)}$, $k_{ai}^{(2)}$ and $k_{ai}'^{(2)}$ can be deter-mined. The values for b_0 and b_1 obtained in this way, for various values of ρ_{CH_3I} are given in Table 1, and are plotted as functions of ρ_{CH_3I} in Figs. 3a and 3b, respectively. A nonlinear regression on the data of Figs. 3a and 3b using Eq. (10) shows that b_0 and b_1 are quadratically dependent upon ρ_{CH_3I}, thus justifying the use of pathway 2. Furthermore, these regression analyses determine the effective rate constants for electron attachment and associative ionization, which are also given in Table 1. (The electron attachment rate constant $k_{ea}^{(2)}$ obtained here should be equivalent to that determined from the analysis of pure CH_3I (cf. Table 1 in [14]) and CH_3I/Ar (cf. Table 4 in [14]). Similarly, the value of the associative ionization constant $k_{ai}^{(2)}$ determined from this system should be equivalent to $k_{ai}^{(2)}$ obtained from pure CH_3I (cf. Table 1 in [14]), CH_3I/Ar (cf. Table 4 in [14]) and CH_3I/SF_6 (cf. Table 5 in [14])). In all of these cases, the measured rate constants agree with one another.)

As mentioned above, an explanation of the density dependence of the $CH_3I/c\text{-}C_4F_8$ subthreshold

Table 2
(a) The constant regression coefficients b_0 and (b) the linear regression coefficients b_1 determined from a pressure study of the subthreshold photoionization structure of $CH_3I/c\text{-}C_4F_8$ as a function of ρ_{CH_3I} (10^{19} cm^{-3}).

a. b_0

ρ_{CH_3I}	10d	11d	12d	13d	14d
0.00024	0.00	0.0055	0.0090	0.013	0.017
0.012	0.0075	0.028	0.046	0.065	0.086
0.061	0.041	0.15	0.26	0.37	0.51
0.12	0.090	0.33	0.56	0.83	1.2
0.37	0.46	1.4	2.4	3.9	5.8
Effective rate constants (arbitrary units) [a]					
$k_{ea}^{(1)}$	0.38	1.7	2.8	4.0	5.3
$k_{ai}^{(2)}$	1.1	3.7	7.5	14	24

b. b_1

ρ_{CH_3I}	10d	11d	12d	13d	14d
0.00024	0.00	0.0061	0.012	0.024	0.041
0.012	0.011	0.033	0.064	0.12	0.21
0.061	0.084	0.19	0.35	0.66	1.1
0.12	0.23	0.45	0.76	1.4	2.3
0.37	1.4	2.3	3.2	5.2	8.2
Effective rate constants (arbitrary units) [a]					
$k_{ai}^{(1)}$	0.80	2.6	5.2	10	17
$k_{ai}'^{(2)}$	8.9	9.3	9.9	11	12

The effective rate constants $k_{ai}^{(1)}$, $k_{ai}^{(2)}$ and $k_{ai}'^{(2)}$ are from least-square second-order polynomial fits to Eq. (11), as shown in Figs. 3a′ and 3b′. The rate constant $k_{ea}^{(1)}$ results from subtracting the value for $k_{ea}^{(2)}$ obtained from CH_3I/CF_4 (cf. Table 1) from the first-order regression coefficient of the least-square fit of b_0 (see text for details).

photoionization structure requires both pathways 1 and 2 and, therefore, b_0 and b_1 should be modeled by Eq. (11). In Figs. 3a′ and 3b′, respectively, b_0 and b_1 for the CH_3I/c-C_4F_8 system are plotted as functions of ρ_{CH_3I}. These values are given in Table 2, along with the effective rate constants $k_{ea}^{(1)}$, $k_{ai}^{(1)}$, $k_{ai}^{(2)}$ and $k'_{ai}{}^{(2)}$ obtained from a least-squares second-order polynomial fit of b_0 and b_1 to Eq. (11). (We must point out that, from the regression analysis of b_0, only $k_{ai}^{(2)}$ and the sum of the electron attachment rate constants $k_{ea}^{(2)} + k_{ea}^{(1)}$ are obtained. However, since $k_{ai}^{(2)}$ obtained from this analysis agrees, to within experimental error, with $k_{ai}^{(2)}$ as determined from CH_3I/CF_4 (cf. Table 1), we have used the $k_{ea}^{(2)}$ value determined from CH_3I/CF_4 in order to obtain the $k_{ea}^{(1)}$ values reported here.)

Since $k_{ea}^{(1,2)}$ is proportional to the (saturated) electron attachment cross-section which, in turn, scales as the principal quantum number n of the dopant Rydberg state [24], $k_{ea}^{(1,2)}$ should vary linearly with n. The associative ionization rate constants $k_{ai}^{(1,2)}$ and $k'^{(2)}_{ai}$, on the other hand, are determined by molecular interactions which are dependent upon the excited state polarizability of the dopant [25]. Since the Rydberg state polarizability scales as n^7 [24], $k_{ai}^{(1,2)}$ and $k'^{(2)}_{ai}$ should also scale as n^7. Therefore, the n-dependence of the effective rate constants can be used to substantiate further the choice of pathways [11,12,14,15].

In Fig. 4a, we plot versus n the effective rate constant for electron attachment to c-C_4F_8 (i.e., $k_{ea}^{(1)}$ (c-C_4F_8)) and for electron attachment to CH_3I (i.e., $k_{ea}^{(2)}$ (CH_3I)). The associative ionization rate constant for CH_3I/c-C_4F_8 heteromolecular dimerization (i.e., $k_{ai}^{(1)}$ (c-C_4F_8)) and for CH_3I homomolecular dimerization (i.e., $k_{ai}^{(2)}$ (CH_3I)) are plotted as functions of n^7 in Fig. 4b. Similarly, in Fig. 4c, the perturber-stabilized associative ionization rate constants $k'^{(2)}_{ai}$ for CH_3I/P (P = CF_4, c-C_4F_8) are plotted versus n^7. (We have also included in Figs. 4a and 4b, respectively, the rate constants for electron attachment to SF_6 (i.e., $k_{ea}^{(1)}$ (SF_6)) and CH_3I/SF_6 heteromolecular dimerization (i.e., $k_{ai}^{(1)}$ (SF_6)) obtained from CH_3I/SF_6 measurements [14]. In Fig. 4c, $k'^{(2)}_{ai}$ obtained from CH_3I/Ar and CH_3I/SF_6 [14] are also included.) Clearly, $k_{ea}^{(1,2)}$ is linearly dependent on n, and $k_{ai}^{(1,2)}$ and $k'^{(2)}_{ai}$ are directly proportional to n^7. We can conclude, therefore, that electron attachment (i.e., Eqs. (1) and (3)) and associative ionization (i.e., Eqs. (2), (4) and (5)) are sufficient to explain the density dependence of the subthreshold photocurrent observed in these systems.

Fig. 4a also shows that $k_{ea}^{(1)}$ (SF_6) > $k_{ea}^{(1)}$ (c-C_4F_8) > $k_{ea}^{(2)}$ (CH_3I). If the electron attachment rate constant increases linearly with increasing stability of the molecular anion, then normalization of $k_{ea}^{(1,2)}$ to the electron affinity of the neutral species involved in anion formation (i.e., CH_3I, c-C_4F_8, SF_6) should result in a single linear correlation. In Fig. 5a, we present $k_{ea}^{(1,2)}$ normalized in this way to electron

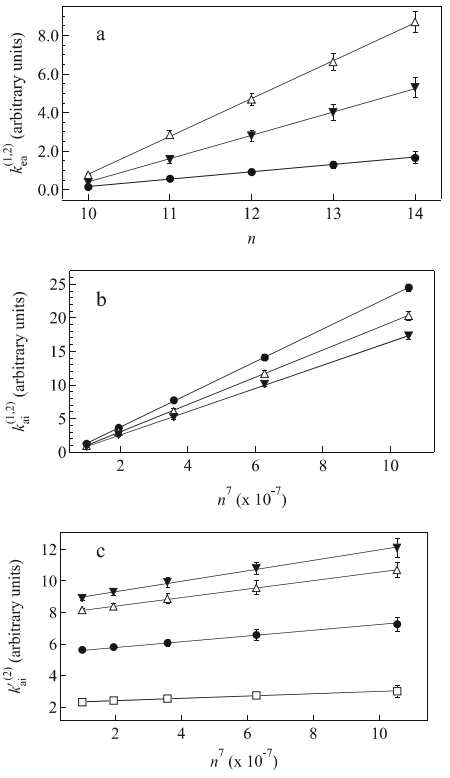

Fig. 4. **(a)** Effective rate constants $k_{ea}^{(1,2)}$ for electron attachment to c-C_4F_8 (i.e., Eq. (1) and Table 2), CH_3I (i.e., Eq. (3) and Table 1) and SF_6 [14] plotted vs. CH_3I excited-state principal quantum number n. (▼) c-C_4F_8, (●) CH_3I and (△) SF_6. **(b)** Effective rate constants $k_{ai}^{(1,2)}$ for associative ionization of CH_3I with c-C_4F_8 (i.e., Eq. (2) and Table 2), with CH_3I (i.e., Eq. (4) and Table 1), and with SF_6 [14] plotted vs. n^7. (▼) c-C_4F_8, (●) CH_3I and (△) SF_6. **(c)** Effective rate constants $k'^{(2)}_{ai}$ for the perturber-stabilized associative ionization of CH_3I (i.e., Eq. (5)) plotted vs. n^7. (▼) c-C_4F_8 (cf. Table 2), (●) CH_3I (cf. Table 1), (△) SF_6 [14] and (□) Ar [14]. The solid lines are linear least-square fits to the data. The error bars for the effective rate constants result from the assumption of a variance of ± 1 standard deviation in both the fitting of the subthreshold peaks and the regression analysis used to obtain these rate constants. See text for discussion.

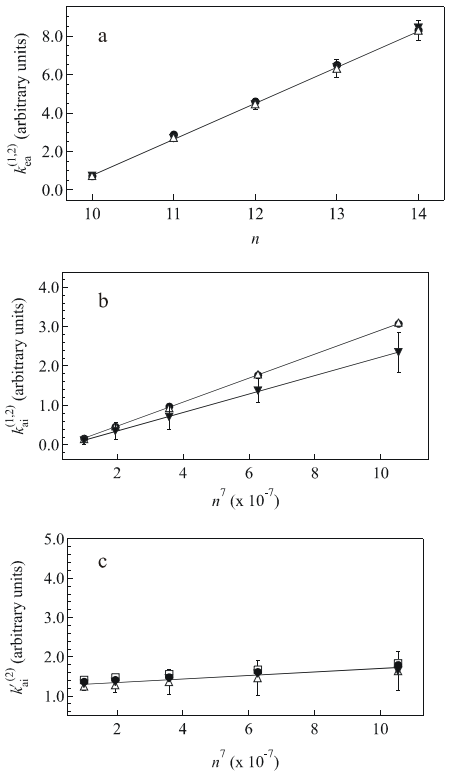

Fig. 5. **(a)** The effective rate constants $k_{ea}^{(1,2)}$ for c-C_4F_8 (▼), CH_3I (●) and SF_6 (△) normalized to the electron affinity of c-C_4F_8, CH_3I and SF_6, respectively. **(b)** The effective rate constants $k_{ai}^{(1,2)}$ for c-C_4F_8 (▼), SF_6 (△) and CH_3I (●) normalized to the ground-state polarizability of c-C_4F_8, SF_6 and CH_3I, respectively. **(c)** The relative rate constants $k_{ai}'^{(2)}$ for c-C_4F_8 (▼), CF_4 (●), Ar (□) and SF_6 (△) normalized to the ground-state polarizability of the perturber. The error bars shown for the effective rate constants are the maximum errors from Fig. 4. See text for the values of the electron affinities and ground-state polarizabilities used.

affinity and plotted as a function of n. This figure shows, to within experimental error, that one correlation line does indeed result. (In Fig. 5a, $k_{ea}^{(1)}$ (c-C_4F_8), $k_{ea}^{(2)}$ (CH_3I) and $k_{ea}^{(1)}$ (SF_6) are normalized to the following electron affinities (eV): c-C_4F_8,0.630 [26]; CH_3I, 0.20 [27]; and SF_6, 1.05 [28].)

From Fig. 4b, $k_{ai}^{(2)}$ (CH_3I) > $k_{ai}^{(1)}$ (SF_6) > $k_{ai}^{(1)}$ (c-C_4F_8), thus indicating that homomolecular CH_3I dimerization (i.e., Eq. (4)) is more favorable than heteromolecular CH_3I/SF_6 dimerization which, in turn, is more favorable than heteromolecular CH_3I/c-C_4F_8 dimerization. The associative ionization rate must depend upon the polarizability of the ground-state molecule in the dimer pair, albeit in ways that are sensitively dependent upon the nature of the potentials chosen to model these (10^{-24} cm^3): CH_3I , 7.97 [29]; c-C_4F_8, 7.37 [30]; and SF_6, 6.54 [31].) Thus, dimerization involving c-C_4F_8 is not as efficient as dimerization involving the more spherical molecules CH_3I and SF_6.interactions [18]. Therefore, if we assume for simplicity a linear dependence of the associative ionization rate constant on the polarizability of the ground-state molecule involved in dimerization, normalization by this polarizability should collapse $k_{ai}^{(1,2)}$ to a single correlation line. Fig. 5b shows that this does in fact hold for CH_3I and for CH_3I/SF_6 [14], but not for CH_3I/c-C_4F_8. (In Fig. 5b, we have normalized to the following polarizabilities

Finally, under the assumption that the perturber-stabilized associative ionization rate constants are also linearly dependent on the ground-state polarizability of the perturber, $k_{ai}'^{(2)}$ should collapse to a single linear correlation for all perturbers. That this is the case for CH_3I/P (P = CF_4, c-C_4F_8, Ar [14] and SF_6 [14]) is shown in Fig. 5c (where we have normalized $k_{ai}'^{(2)}$ to the following polarizabilities (10^{-24} cm^{-3}): CF_4, 3.838 [32]; c-C_4F_8, 7.37 [29]; Ar, 1.6411 [33]; and SF_6, 6.54 [31]).

In summary, subthreshold photoionization spectra of CH_3I/P (P = CF_4, c-C_4F_8) for variations in ρ_{CH_3I} and ρ_P have been presented. The subthreshold photocurrent in CH_3I/CF_4 was shown to follow pathway 2 (i.e., Eqs. (3) - (5) and (7)), while the CH_3I/c-C_4F_8 subthreshold photocurrent proceeds through both pathways 1 and 2 simultaneously (i.e., Eqs. (1) - (5) and (8)). Thus the halocarbon CF_4 is similar in behavior to Ar [12,14], whereas c-C_4F_8 is similar to SF_6 [11,14]. By systematically varying both ρ_{CH_3I} and ρ_P, the effective rate constants for electron attachment and associative ionization were determined. We also demonstrated that the effective rate constant for electron attachment to CH_3I (i.e., $k_{ea}^{(2)}$) obtained from CH_3I/CF_4 agrees well with that obtained from both pure CH_3I [14] and CH_3I/Ar [14]. Moreover, the CH_3I homomolecular dimerization effective rate constant (i.e., $k_{ai}^{(2)}$) obtained from CH_3I/CF_4 and CH_3I/c-C_4F_8 agrees, to within experimental error, with the same constant as determined from pure CH_3I [14], CH_3I/Ar [14] and CH_3I/SF_6 [14], thus demonstrating the consistency of these analyses.

It was also shown that $k_{ea}^{(1,2)}$, $k_{ai}^{(1,2)}$ and $k_{ai}'^{(2)}$ scale in a simple fashion with respect to the principal quantum number n of the CH_3I Rydberg state. One can conclude,

therefore, that the mechanisms of (saturated) electron attachment and associative ionization are sufficient to explain the behavior of the subthreshold photocurrent in CH_3I/CF_4 and $CH_3I/c\text{-}C_4F_8$. Furthermore, the variation in the effective rate constants for electron attachment to CH_3I (i.e., $k_{ea}^{(2)}$) and to $c\text{-}C_4F_8$ (i.e., $k_{ea}^{(1)}$) was shown to scale linearly with electron affinity. However, comparison of the associative ionization effective rate constant (i.e., $k_{ai}^{(1,2)}$) for CH_3I, $c\text{-}C_4F_8$ and SF_6 [14] showed that heteromolecular dimerization of CH_3I to $c\text{-}C_4F_8$ is less efficient than dimerization either to CH_3I or to SF_6. Finally, the perturber-stabilized associative ionization rate constant $k_{ai}^{\prime(2)}$ was also shown to be directly proportional to the ground-state polarizability of the perturber.

Acknowledgments

This work was conducted at the University of Wisconsin Synchrotron Radiation Center (NSF DMR 95-31009) and was supported by a grant from the Louisiana Board of Regents Support Fund (LEQSF (1997-00)-RD-A-14).

References

[1] V. S. Ivanov, F. I. Vilesov, Opt. Spectrosc. 36 (1974) 602.
[2] V. S. Ivanov, F. I. Vilesov, Opt. Spektrosc. 36 (1974) 1023.
[3] V. S. Ivanov, F. I. Vilesov, Opt. Spectrosc. 39 (1975) 487.
[4] V. S. Ivanov, F. I. Vilesov, Opt. Spektrosc. 39 (1975) 857.
[5] A. M. Köhler, Ph.D. Dissertation, University of Hamburg, Hamburg, 1987.
[6] I. T. Steinberger, U. Asaf, G. Ascarelli, R. Reininger, G. Reisfeld, M. Reshotko, Phys. Rev. A 42 (1990) 3135.
[7] U. Asaf, I. T. Steinberger, J. Meyer, R. Reininger, J. Chem. Phys. 95 (1991) 4070.
[8] U. Asaf, J. Meyer, R. Reininger, I. T. Steinberger, J. Chem. Phys. 96 (1992) 7885.
[9] J. Meyer, U. Asaf , R. Reininger, Phys. Rev. A 46, 1673 (1992).
[10] C. M. Evans, R. Reininger, G. L. Findley, Chem. Phys. 297 (1998) 127.
[11] C. M. Evans, R. Reininger, G. L. Findley, Chem. Phys. 241 (1999) 239.
[12] C. M. Evans, R. Reininger, G. L. Findley, Chem. Phys. Lett. 322 (2000) 465.
[13] C. M. Evans, E. Morikawa and G. L. Findley, Chem. Phys. Lett, submitted.
[14] C. M. Evans, E. Morikawa, G. L. Findley, Chem. Phys., submitted.
[15] C. M. Evans, J. D. Scott, F. H. Watson, G. L. Findley, Chem. Phys. 260 (2000) 225.
[16] A. Rosa, I. Szamrej, J. Phys. Chem. A 104 (2000) 67.
[17] D. M. Manos, D. L. Flamm, Plasma Etching, Academic Press, Boston, 1989.
[18] L. E. Kline, M. J. Kushner, Crit. Rev. Solid State Mater. Sci. 16 (1989) 1.
[19] L. G. Christophorou, J. K. Olthoff, M. V. V. S. Rao, J. Phys. Chem. Ref. Data 25 (1996) 1341.
[20] A. K. Al-Omari, Ph.D. Dissertation, University of Wisconsin-Madison, Wisconsin, 1996.
[21] A. K. Al-Omari and R. Reininger, J. Chem. Phys. 103 (1995) 506.
[22] A. M. Köhler, R. Reininber, V. Saile, G. L. Findley, Phys. Rev. A 35 (1987) 79.
[23] J. Meyer, R. Reininger, U. Asaf and I. T. Steinberger, J. Chem. Phys. 94 (1991) 1820.
[24] T. F. Gallagher, Rydberg Atoms, Cambridge University Press, Cambridge, 1994.
[25] J. O. Hirschfelder, C. F. Curtiss, R. B. Bird, Molecular Theory of Gases and Liquids, Wiley, New York, 1964.
[26] T. M. Miller, R. A. Morris, A. E. S. Miller, A. A. Viggiano, J. F. Paulson, Int. J. Mass. Spectrom. Ion Proc. 135 (1994) 195.
[27] P. S. Drzaic, J. Marks, J. I. Brauman, in Gas Phase Ion Chemistry, Vol. 3, M. T. Bowers, Ed. Academic Press, Orlando, 1984, p. 167.
[28] E. P. Grimsrud, S. Chowdhury, P. Kebarle, J. Chem. Phys. 85 (1985) 4989.
[29] A. A. Maryott, F. Buckley, U. S. NBS No. 537, 1953.
[30] L. Kevan, J. H. Futrell, J. Chem. Soc. Faraday Trans. 2 68 (1972) 1742.
[31] R. D. Nelson, R. H. Cole, J. Chem. Phys. 54 (1971) 4033.
[32] T. K. Bose, J. S. Sochanski, R. H. Cole, J. Chem. Phys. 57 (1972) 3592.
[33] A. C. Newell, R. D. Baird, J. Appl. Phys. 36 (1965) 3751.